Remote Sensing of Environment 124 (2012) 348–359

Contents lists available at SciVerse ScienceDirect

Remote Sensing of Environment

journal homepage: www.elsevier.com/locate/rse

Large-area landslide detection and monitoring with ALOS/PALSAR imagery data over Northern California and Southern Oregon, USA

Chaoying Zhao [a,b], Zhong Lu [c,*], Qin Zhang [a,b], Juan de la Fuente [d]

[a] College of Geology Engineering and Geomatics, Chang'an University, Xian Shaanxi, China
[b] Key Laboratory of Western China's Mineral Resources and Geological Engineering, Ministry of Education, No.126 Yanta Road, Xian, Shaanxi, China
[c] U.S. Geological Survey, Vancouver, Washington, USA
[d] U.S. Forest Service, 1711 Fairlane Road, Yreka, California, 96097 USA

ARTICLE INFO

Article history:
Received 14 March 2012
Received in revised form 23 May 2012
Accepted 26 May 2012
Available online xxxx

Keywords:
Landslide
Monitoring
Detection
ALOS/PALSAR
Synthetic aperture radar (SAR)
Interferometric SAR (InSAR)

ABSTRACT

Multi-temporal ALOS/PALSAR images are used to automatically investigate landslide activity over an area of ~200 km by ~350 km in northern California and southern Oregon. Interferometric synthetic aperture radar (InSAR) deformation images, InSAR coherence maps, SAR backscattering intensity images, and a DEM gradient map are combined to detect active landslides by setting individual thresholds. More than 50 active landslides covering a total of about 40 km^2 area are detected. Then the short baseline subsets (SBAS) InSAR method is applied to retrieve time-series deformation patterns of individual detected landslides. Downslope landslide motions observed from adjacent satellite tracks with slightly different radar look angles are used to verify InSAR results and measurement accuracy. Comparison of the landslide motion with the precipitation record suggests that the landslide deformation correlates with the rainfall rate, with a lag time of around 1–2 months between the precipitation peak and the maximum landslide displacement. The results will provide new insights into landslide mechanisms in the Pacific Northwest, and facilitate development of early warning systems for landslides under abnormal rainfall conditions. Additionally, this method will allow identification of active landslides in broad areas of the Pacific Northwest in an efficient and systematic manner, including remote and heavily vegetated areas difficult to inventory by traditional methods.

Published by Elsevier Inc.

1. Introduction

Landslides are defined as the movement of a mass of rock, debris or earth down a slope (Cruden, 1991), and can result in enormous casualties and huge economic losses in mountainous regions. Additionally, landslides in the Pacific Northwest can damage habitat utilized by valuable fish species, such as salmon and steelhead. In recent years, many different mapping techniques have been implemented for the cartographic representation of landslide movement. These include landslide inventories, landslide displacement inventories, landslide hazard assessments, and landslide vulnerability assessments (Parise, 2001). Risk analysis and assessment have also become important tools in addressing uncertainty inherent in landslide hazards (Dai et al., 2002). In addition, susceptibility zoning involves the spatial distribution and rating of the terrain units according to their propensity to produce landslides (Fell et al., 2008). Among all of these studies, mapping landslide deformation is fundamental for the assessment and reduction of landslide hazards and risks. In comparison to the traditional investigation and reconnaissance methods, such as GPS, spirit leveling, tilting, optical remote sensing, geological and geophysical investigation methods (Ding et al., 1998; Thompson & Cierlitza, 1993), the interferometric synthetic aperture radar (InSAR) technique has great advantages due to its broad coverage and its high spatial (and sometime temporal) resolution under all weather conditions (Massonnet & Feigl, 1998).

The InSAR technique has been used in various landslide studies, not only for location detection (Bulmer et al., 2006; Cascini et al., 2010; Farina et al., 2006; Pierson & Lu, 2009), but also for deformation monitoring. Various InSAR techniques have been employed, including the traditional differential InSAR method (Calabro et al., 2010; Catani et al., 2005; Strozzi et al., 2005), the short baseline subsets (SBAS) InSAR method (Berardino et al., 2003), the corner reflector InSAR (Fu et al., 2010; Xia et al., 2004), the persistent scatterer InSAR technique (Colesanti et al., 2003; Hilley et al., 2004; Vladimir & Jan, 2011) and ground based InSAR technique (Leva et al., 2003). InSAR-derived landslide deformation patterns further provide insights into the dynamics of landslides, including the interaction of landslides and tectonic motions and the deformation characteristics in relation to the El Nino phenomenon (Calabro et al., 2010; Colesanti et al., 2003; Hilley et al., 2004). However, the application of the InSAR technique to landslide investigations is still a challenging topic. It is difficult to map and monitor landslides in forested regions due to volume and temporal decorrelation, atmospheric delay anomalies, artifacts induced by near surface moisture changes

* Corresponding author. Tel.: +1 360 993 8911; fax: +1 360 993 8981.
E-mail address: lu@usgs.gov (Z. Lu).

0034-4257/$ – see front matter. Published by Elsevier Inc.
doi:10.1016/j.rse.2012.05.025

and decorrelation due to large deformation gradients (Ferretti et al., 2007; Hanssen, 2001; Massonnet & Feigl, 1998; Samsonov et al., 2011; Yun et al., 2007; Zebker & Villasenor, 1992). In addition, the side-looking SAR imaging geometry causes layover and shadow in mountainous regions. Furthermore, large scale phase trends resulting from baseline errors and atmospheric artifacts make it difficult to detect and monitor landslides over a large region.

In this study, we first introduce a method for automatic detection of slowly moving landslides using InSAR products (Lu et al., 2010), including InSAR coherence maps, SAR intensity images, deformation maps and digital elevation models (DEM). We then apply this method to map active landslides in a large region in the southern Oregon and northern California. The detected landslides are verified by independent InSAR observations from adjacent satellite tracks and some in-situ data. The spatial segmentation for a specific landslide is analyzed in detail, the temporal time-series deformation results are achieved using SBAS technique, and the accuracy of deformation measurements is verified using two independent InSAR observations from adjacent satellite tracks. Finally, the correlation between the time-series landslide motion derived and the precipitation record is analyzed.

2. Data and study area

The study region, covering an area of ~200 km by ~350 km in northern California and southern Oregon (Fig. 1), is composed of penetratively sheared metasedimentary interbedded sandstone and

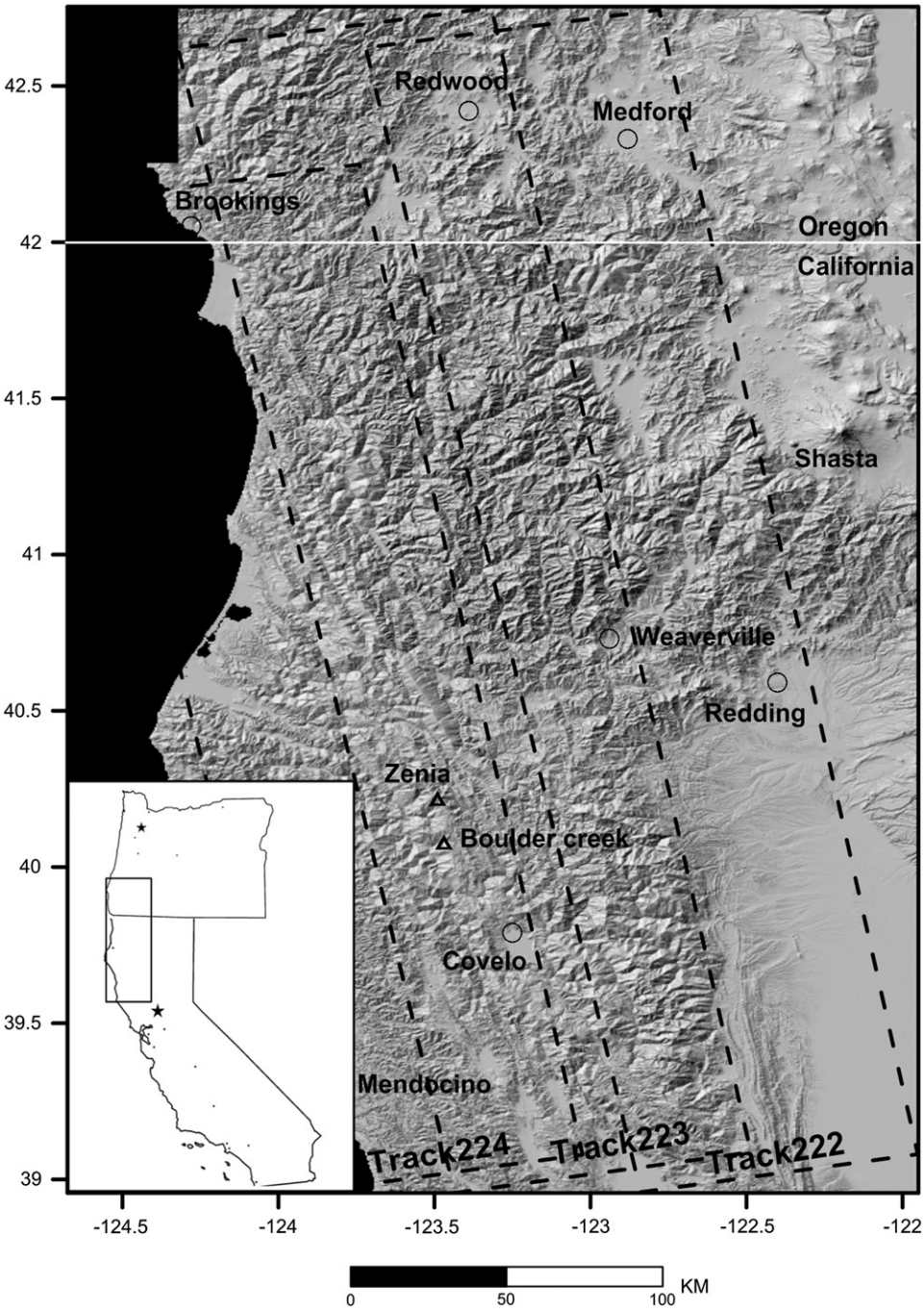

Fig. 1. Shaded-relief image of the study area over northern California and southern Oregon, USA. Dashed polygons represent the coverage of SAR images from three overlapping ascending ALOS/PALSAR tracks 222, 223 and 224. The inset is a sketch map of California and Oregon, and the rectangle represents the study region.

argillite of the Franciscan Complex, a Jurassic–Cretaceous accretionary prism complex renowned for earthflows and deep-seated landsliding (Iverson & Major, 1987). Taking the Eel River basin in northern California as an example, some of the most extensive earthflow activity occurs along the main stream and its tributaries. Highly erodible Central Belt melange and high seasonal rainfall predispose this section to ubiquitous earthflows (Mackey et al., 2009 and references therein).

We collected 3 tracks of ascending L-band ALOS/PALSAR images over northern California and southern Oregon (Fig. 1). In the azimuth direction (nearly north–south), each track consists of about 5 to 6 consecutive image frames. The SAR data span from early 2007 to late 2010 and a total of 200 frames of SAR images are utilized. In the InSAR processing and the terrain gradient calculation, the 1-arc-second SRTM is used (Farr et al., 2007). The holes (non-value pixels) in the SRTM DEM are filled using the national elevation dataset (NED) DEM (Gesch, 1994). The fine beam double polarization (FBD) images are oversampled to the pixel spacing of the fine beam single polarization (FBS) images. A multilook factor of 10 (2 pixels in range and 5 pixels in azimuth directions) is applied to generate InSAR images at a spatial resolution of ~15 m in both directions. Images at this resolution have the potential to detect small-scale landslides and also are better suited to map landslides with large deformation gradients (Sandwell et al., 2008; Yun et al., 2007). After screening interferogram coherence, we have selected 16 interferograms from track 222, 28 from track 223, and 10 from track 224 (Table 1). Most of the accepted interferograms have time separations of 138 days or less and spatial baselines of 1000 m or less. So, we have generated a total of 54 interferograms from three adjacent satellite tracks (Table 1).

Table 1
ALOS/PALSAR interferometric pairs from 3 different tracks.

No.	Master	Slave	Perpendicular baseline (m)	Days	Track no.
1	20070713	20070828	296.1	46	222
2	20070713	20071013	750.2	92	
3	20070713	20071128	833.9	138	
4	20070828	20071013	454.1	46	
5	20070828	20071128	537.8	92	
6	20071013	20071128	83.7	46	
7	20080228	20080414	400.4	46	
8	20080228	20080530	239.4	92	
9	20080414	20080530	−161.1	46	
10	20091018	20100118	515.3	92	
11	20100118	20100420	811.6	92	
12	20100118	20100605	999.9	138	
13	20100420	20100605	188.3	46	
14	20100420	20100721	229.8	92	
15	20100605	20100721	41.5	46	
16	20100721	20101206	655.0	138	
1	20070314	20070429	490.2	46	223
2	20070314	20070614	−17.4	92	
3	20070314	20070730	479.2	138	
4	20070314	20070914	661.6	184	
5	20070429	20070614	−507.6	46	
6	20070429	20070730	−11.0	92	
7	20070429	20070914	171.4	138	
8	20070614	20070730	496.6	46	
9	20070614	20070914	679.0	92	
10	20070730	20070914	182.3	46	
11	20070730	20080130	1380.4	184	Low quality
12	20070914	20080130	1198.1	138	Low quality
13	20080130	20080501	944.6	92	
15	20081101	20090201	702.2	92	
16	20081101	20090319	1200.4	138	Low quality
17	20090201	20090319	498.3	46	
18	20090201	20090619	836.8	138	
19	20090201	20090804	433.4	184	
20	20090319	20090619	338.5	92	
21	20090319	20090804	−64.9	138	
22	20090619	20090804	−403.4	46	
23	20090619	20091220	1003.6	184	Low quality
24	20090804	20091220	1407.0	138	Low quality
25	20091220	20100322	1009.1	92	Low quality
26	20091220	20100507	1157.2	138	Low quality
27	20100322	20100507	148.1	46	
28	20101223	20110325	1110.2	92	Low quality
1	20070516	20070701	176.4	46	224
2	20070516	20070816	462.1	92	
3	20070701	20070816	285.7	46	
4	20071116	20080101	−112.0	46	
5	20100106	20100221	688.6	46	
6	20100106	20100408	863.7	92	
7	20100221	20100408	175.1	46	
8	20100221	20100524	215.7	92	
9	20100408	20100524	40.7	46	
10	20101124	20110109	443.8	46	

3. Methodology

3.1. Landslide detection with InSAR

InSAR images and derived products have proven useful in mapping and characterizing ground deformation and landscape changes (Lu et al., 2010). In this study, the deformation images, along with the InSAR coherence maps, SAR intensity images and terrain slope maps are combined to map active landslides reliably.

Fig. 2 is the flow chart outlining the procedure for detecting active landslides based on InSAR products. For a given interferometric pair, we generate an unwrapped differential interferogram, a coherence image, a mean SAR backscattering intensity image based on the backscattering returns from the master and slave images, and a DEM gradient map. The DEM has a threefold application in the landslide detection processing. The first is to simulate the topographic phase to obtain the deformation interferograms. The second is to refine the baseline using the coregistered DEM and unwrapped phase in SAR coordinates (Rosen et al., 1996). The last is to generate the DEM gradient map, which is one of the input layers for landslide detection. The unwrapped interferogram is corrected using the refined baseline, and a large-scale band-pass filter is applied to remove the atmospheric artifact. Based on trial analysis, band-pass frequency values of 0.005 and 0.01 in slant range and azimuth directions are chosen for the interferograms used in this study. Coherence maps are created from the corrected unwrapping phase and have taken into account the localized phase gradient using a moving window of 5 by 5 pixels (Zebker & Chen, 2005). For each InSAR pair, a total of 4 data layers (deformation, coherence, intensity and DEM gradient maps) are combined to detect active landslide candidates by thresholds. The main threshold is the deformation value used to detect active landslides. Absolute LOS displacement value of 1 cm is set as the threshold based on trial and error analyses. In order to remove possible deformation artifacts due to DEM, atmosphere, or phase unwrapped errors, a coherence threshold of 0.6 is set to guarantee the reliability of detected landslides, A threshold of −1 dB is set for the SAR intensity to avoid any shadow areas or water bodies. Finally, we also set a threshold of 10° for the DEM gradient based on terrain slopes of some known landslides. Independent interferometric pairs from the same track are then used to confirm the landslide candidates. We apply the same procedure to InSAR pairs from other tracks. Independent observations from adjacent satellite tracks can be used to further validate the mapped landslides. The detected landslides are mosaicked in a final map.

3.2. Landslide deformation monitoring with SBAS InSAR

In order to mitigate the atmospheric artifact and the residual topographic effect during the deformation retrieval step, one of the advanced InSAR techniques termed short baseline subsets (SBAS) InSAR has been frequently applied (Berardino et al., 2002; Lanari et al., 2004;

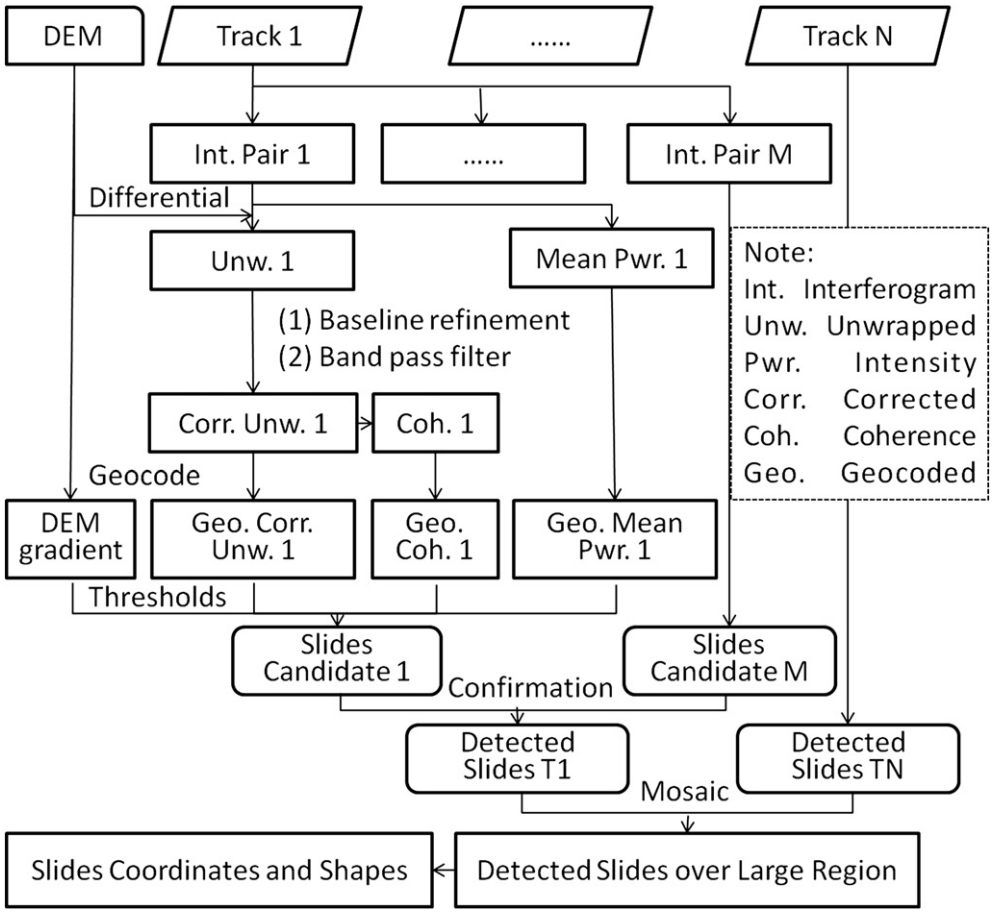

Fig. 2. Flow chart of landslide detection methodology with a multi-interferogram method.

Sansosti et al., 2010). SBAS also works when limited interferometric sets are available (Mora et al., 2003). In order to robustly estimate the topographic error and time-series deformation results, the SBAS procedure has been refined by separating the interferograms into high-quality and low-quality subsets, and iteratively estimating the parameters (Lee et al., 2010). During each iteration, the observation with its residual larger than twice the standard deviation error is rejected.

After quality assurance on interferogram phase unwrapping, interferograms are then segmented into several individual small sections according to the detected landslide coordinates to facilitate SBAS processing. In each image segment, the interferograms are divided into two subsets, namely high-quality sets and low-quality sets. The high quality sets are used to estimate DEM error and linear deformation rate, while all interferograms are used to estimate deformation time series (Lee et al., 2010).

For a given unwrapped interferogram j, the phase at pixel (x, r) (where x and r are the azimuth and slant range coordinates, respectively) computed from the SAR acquisitions at epoch t_A(start time) and t_B(end time) can be written as follows (Berardino et al., 2002):

$$\delta\phi_j(x,r) = \phi(t_B,x,r) - \phi(t_A,x,r) = \delta\phi_j^{defo}(x,r) + \delta\phi_j^{topo}(x,r) + \delta\phi_j^{atm}(x,r) + \delta\phi_j^{noise}(x,r) \quad (1)$$

where, $\delta\phi_j^{defo}$ is slant deformation phase between t_A and t_B;$\delta\phi_j^{topo}$ represents topographic phase error, the impact of which on deformation maps is a function of the perpendicular baseline $B_{\perp j}$, the slant range distance R, look angle θ and DEM error ΔZ;$\delta\phi_j^{atm}$ accounts for temporal atmospheric variation at different SAR acquisition t_A and t_B; the final term $\delta\phi_j^{noise}$ is the other noise sum. The first three terms of the right side of Eq. (1) can be expressed as follows

$$\begin{cases} \delta\phi_j^{defo}(x,r) = \dfrac{4\pi}{\lambda}[d(t_B,x,r) - d(t_A,x,r)] = a_j(x,r)\cdot v + \delta\phi_j^{nl\_defo}(x,r) \\ \delta\phi_j^{topo}(x,r) = \dfrac{4\pi}{\lambda}\dfrac{B_{\perp j}\Delta Z}{R\sin\theta} = b_j(x,r)\cdot\Delta Z \\ \delta\phi_j^{atm}(x,r) = \phi_{atm}(t_B,x,r) - \phi_{atm}(t_A,x,r) \end{cases} \quad (2)$$

where λ is the SAR wavelength, v is the deformation rate, $\delta\phi_j^{nl_defo}(x, r)$is the nonlinear deformation between two SAR acquisition dates. Eq. (1) can then be rewritten in matrix form as follows

$$\delta\phi(x,r) = [A(x,r), B(x,r)]\begin{bmatrix} v \\ \Delta Z \end{bmatrix} + N(x,r) \quad (3)$$

where $A(x,r) = [a_1(x,r) \quad \cdots \quad a_{M1}(x,r)]^T$,$B(x,r) = [b_1(x,r) \quad \cdots b_{M1}(x,r)]^T$, $N(x,r) = \begin{bmatrix} \delta\phi_1^{nl_defo}(x,r) + \delta\phi_1^{atm}(x,r) + \delta\phi_1^{noise}(x,r) \\ \vdots \\ \delta\phi_{M1}^{nl_defo}(x,r) + \delta\phi_{M1}^{atm}(x,r) + \delta\phi_{M1}^{noise}(x,r) \end{bmatrix}$, and $M1$ is the number of high-quality interferograms. The estimated linear deformation rate and DEM error phases are then subtracted from all unwrapped interferograms. Next, the atmospheric phase will be separated by high-pass filtering in temporal domain and low-pass filtering in the spatial domain, because the atmospheric artifacts

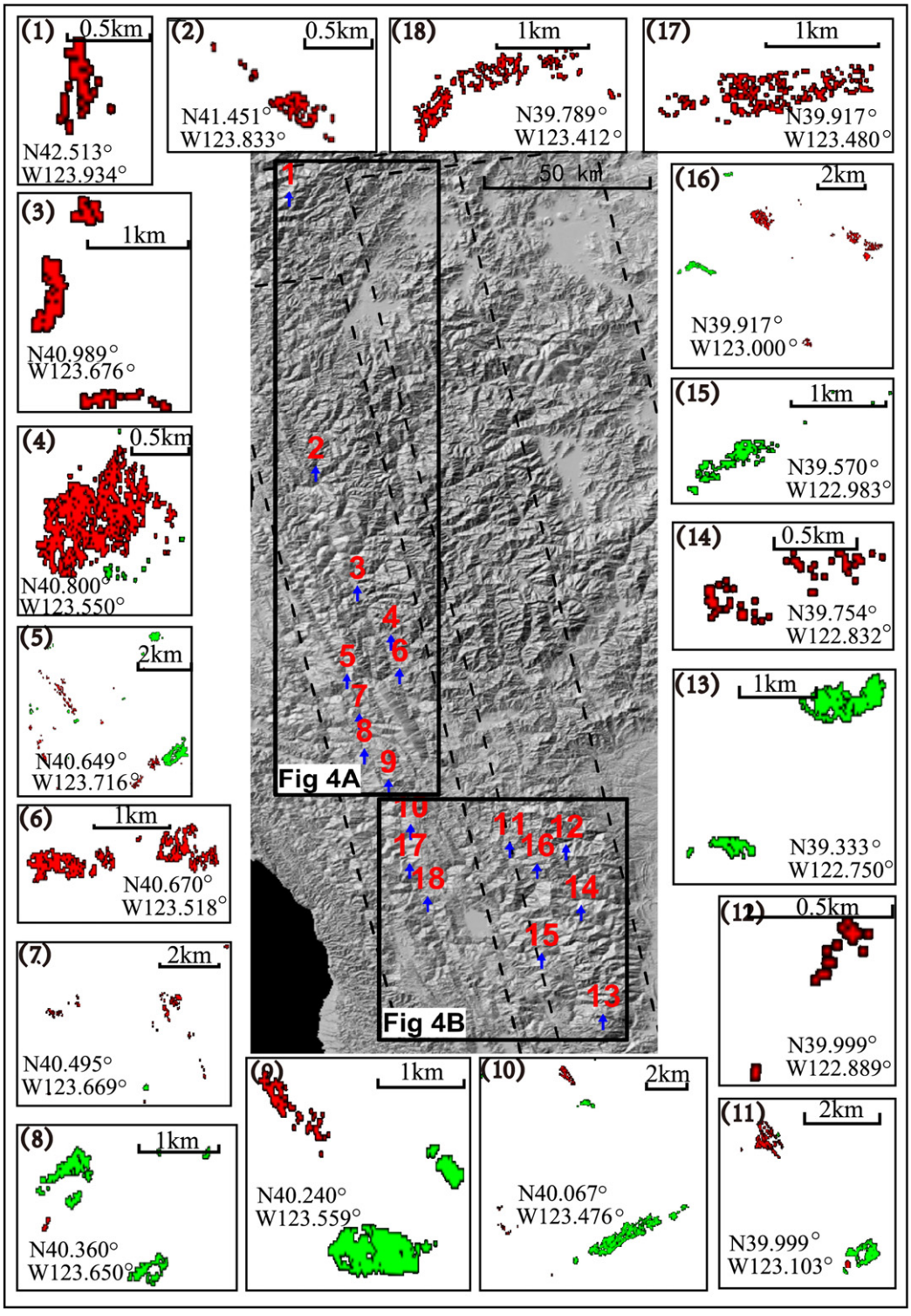

Fig. 3. Distribution of detected landslides. Some examples are shown around the image borders. Slides moving towards the satellite (i.e. those on slopes facing to the west) are shown in green. Slides moving away from the satellite (i.e. those on slopes facing to the east) are shown in red. Arrows indicate the positions of major landslides. Deformation images for the 18 major slides are shown in Fig. 4A and B, respectively. Note the different scales for the DEM image and maps of detected landslides.

are spatially correlated and temporally random (Ferretti et al., 2001). Therefore, after the simultaneous operation of SVD and finite difference smoothing of the atmospheric corrected phase, the nonlinear deformation phase at different SAR acquisition dates will be calculated (Lee et al., 2010; Schmidt & Burgmann, 2003). In the former calculation, if the term $N(x, r)$ is not too small, the estimation of deformation rate and DEM error will be biased. So the former procedure will be processed iteratively. Last, the accumulated deformation series will be achieved as follows

$$\delta\phi_k^{defo}(x,r) = (t_k - t_1)v + \sum_{i=2}^{k} \varphi_i^{nl_defo} \tag{4}$$

where t_1 is the earliest SAR acquisition date. InSAR coherence is poorer when the time interval is larger than about half of a year or the baseline

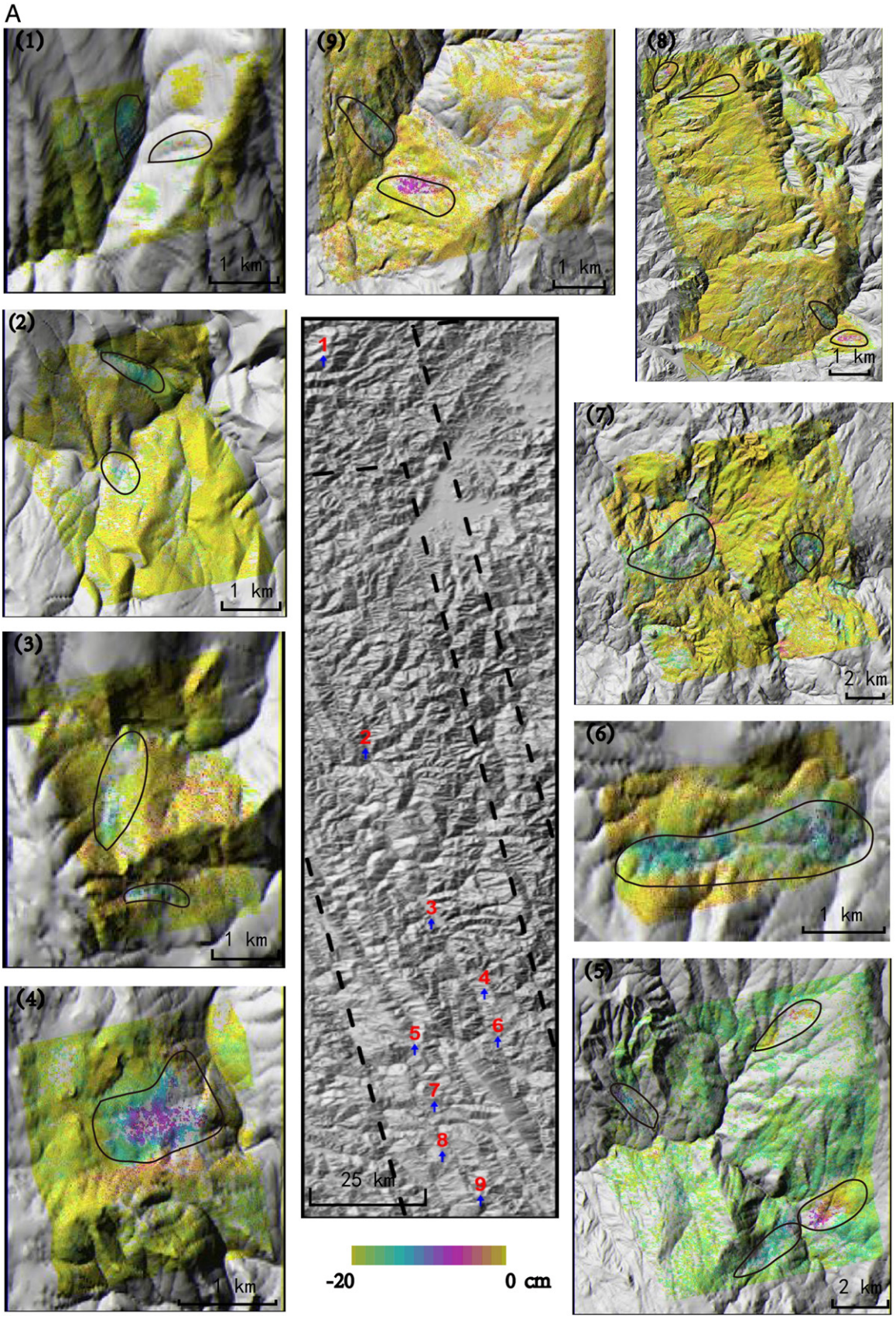

Fig. 4. A. LOS deformation images for 9 selected landslides over 138 days during 20070314 and 20070730 from ALOS/PALSAR track 223. Note the different scales for different maps of detected landslides. B. LOS deformation images for another 9 selected landslides over 138 days during 20070314 and 20070730 from ALOS/PALSAR track 223. Note the different scales for different maps of detected landslides.

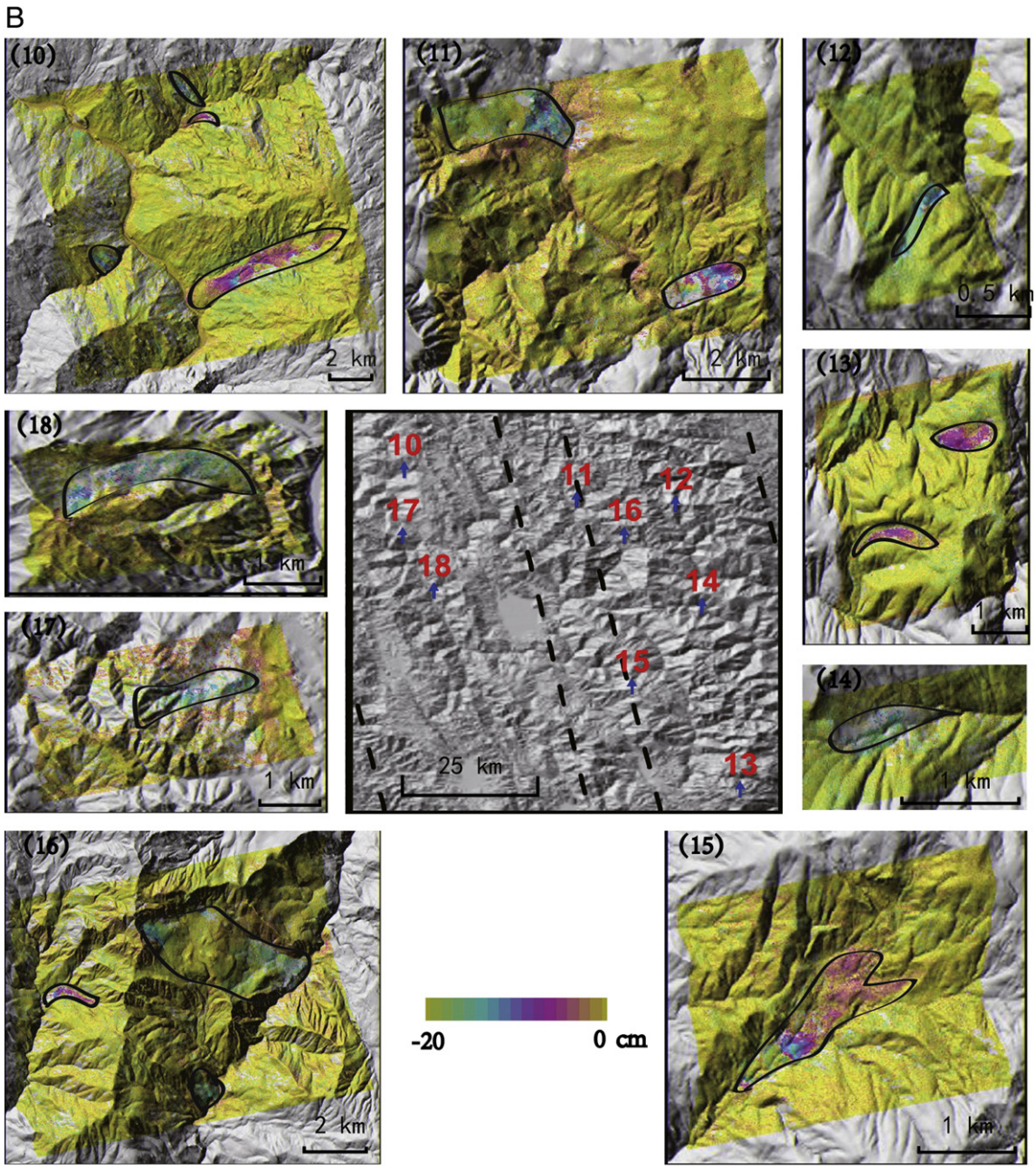

Fig. 4(*continued*).

larger than about 1.2 km. Therefore, temporal gaps exist as we cannot bridge the time-series measurements.

3.3. Along-slope deformation

InSAR can only measure the deformation along the line-of-light (LOS) direction. That is, the InSAR measurement represents the component of ground deformation projected to the LOS direction. With some assumptions, the LOS deformation can be transferred to the measurement from a specific angle and azimuth direction. In this study, we project the LOS deformation to the down-slope direction and then verify the InSAR measurement accuracy based on observations from two independent satellite tracks.

The transformation between the LOS direction and down-slope direction is straight forward. The unit vector of LOS can be defined as follows

$$\vec{r} = \begin{bmatrix} r_{east} \\ r_{north} \\ r_{up} \end{bmatrix} = \begin{bmatrix} -\sin\theta\cos\alpha_s \\ \sin\theta\sin\alpha_s \\ \cos\theta \end{bmatrix} \tag{5}$$

where θ is incidence angle, α_s is the satellite flight azimuth. The unit vector of slope can be defined as follows

$$\vec{u} = \begin{bmatrix} u_{east} \\ u_{north} \\ u_{up} \end{bmatrix} = \begin{bmatrix} -\sin\alpha\cos\varphi \\ -\cos\alpha\cos\varphi \\ \sin\varphi \end{bmatrix} \tag{6}$$

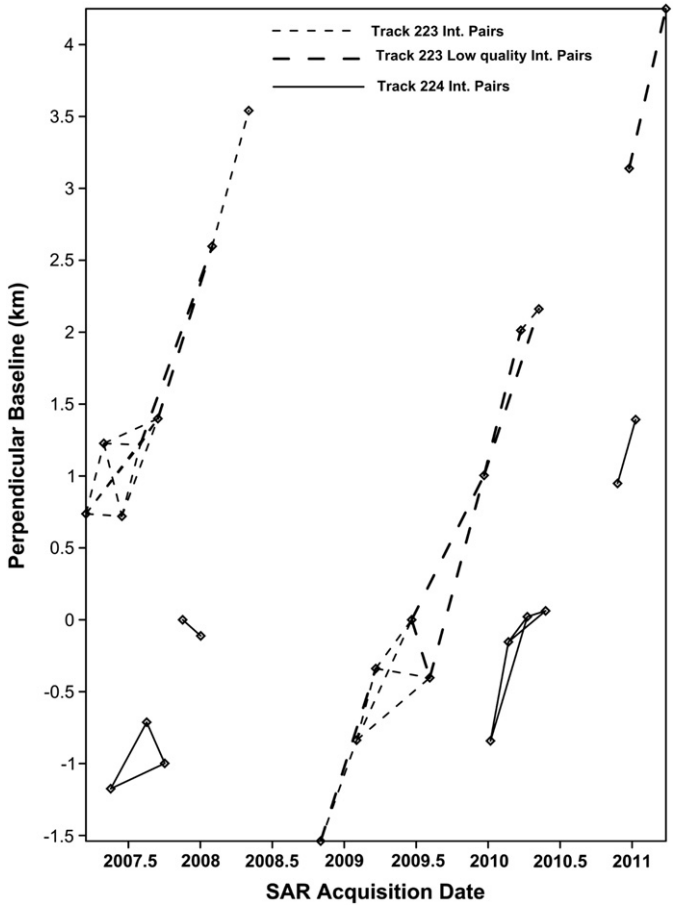

Fig. 5. Configurations of InSAR pairs used for SBAS processing for InSAR images from tracks 223 and 224, respectively.

where α is the slope angle above the horizontal surface, φ is the slope azimuth. So the deformation in the slope direction can be expressed as

$$d_{slope} = {}^{d_{LOS}}\Big/_{\left(r_{east}u_{east}+r_{north}u_{north}+r_{up}u_{up}\right)} \quad (7)$$

4. Results, analyses and discussions

4.1. Landslide location map

The four layers of InSAR products, including the deformation map, the InSAR coherence image, the SAR backscattering intensity image and the DEM gradient map, are used to delineate active landslides based on the procedure outlined in Fig. 2. We set the thresholds for these four datasets as 0.6 for coherence, −1 dB for intensity, 10° for DEM gradient, and 1 cm for LOS deformation. First, active landslides are tentatively identified using independent interferometric results from the same track. Then, landslide candidates from three different satellite tracks are mosaicked together. Some landslide candidates are further cross-validated using independent observations from two adjacent satellite tracks. Fig. 3 shows the distribution of the detected landslides.

Within the investigated area of ~200 km by ~350 km, more than 50 landslides are detected. About 90% of the detected landslides are verified using data from neighboring tracks. Most of the detected landslides have elongated patterns (Fig. 3). The discontinuous portion within each landslide mainly results from the loss of coherence due to large deformation gradients and dense vegetation cover (e.g., (1), (2), (4), (6), (12), (14), (15), (17), and (18) in Fig. 3.). Some insets labeled such as (3), (5), (7), (8), (9), (10), (11), (13), (16) in Fig. 3 contain several separated landslides. The size of the detected landslides ranges from about 0.2 km^2 to more than 10 km^2. Active landslides occupy a total area of over 40 km^2. In this study, only the landslides that deformed more than 1 cm in 46 days and consistently moved between 2007 and 2010 are outlined. In addition, the slides that deform parallel to the ALOS SAR satellite flight direction (9.9° west of north) might be missed because the LOS imaging geometry is less sensitive to the landslide motion in this direction. Furthermore, landslides that fall into the regions of SAR geometry distortions (layovers and shadows) cannot be mapped either. That is, landslides on slopes larger than the ALOS/PALSAR look angle (~38° for most beam modes) cannot be detected. Therefore, our results surely underestimate the active landslides in the study area.

4.2. Landslide deformation maps

In this section, to reduce the computation burden, the time-series deformation histories for 18 detected landslides are calculated one by one using the refined SBAS algorithm (Lee et al., 2010). Fig. 4A and B shows the deformation accumulated over 138 days between 20070314 and 20070730 from interferograms of track 223. The deformation patterns are consistent with the landslide shapes shown in the previous section. The maximum deformation was more than 10 cm in 138 days (Figs. 4A, B, and 7).

4.3. Time-series deformation at Boulder Creek

The Boulder Creek slide (labeled as No. 10 in Fig. 4B) is located about 16 km ESE of Garberville, California, immediately east of the Eel River (Stimely, 2009). The landslide exhibits fresh landform features (pronounced head scarp, well-defined lateral scarps, and very hummocky interior), which is typical of many active earthflows in the Coast Ranges.

The aim of the time-series deformation analysis for this slide is threefold. First, we examine the spatial and temporal characteristics of the landslide movement by focusing on variations in movement rate on different parts of the slide. Second, we verify the InSAR accuracy by comparing two independent results generated from track 223 and track 224. Last, we correlate the nonlinear landslide deformation with local precipitation.

Fig. 5 shows the spatial baselines and temporal separations of InSAR pairs used for SBAS processing. There are 3 subsets of interferograms in track 223 and 4 subsets of interferograms in track 224. For each satellite track, SBAS processing allows us to derive time-series deformation maps by combining interferograms from all subsets (Fig. 5). A total of 8 low-quality interferograms from track 223 are included to densify the time series analysis. Fig. 6 shows the deformation time-series maps of Boulder Creek slide (labeled as No. 10 in Fig. 4B). Four individual landslides can be seen in the upper-central, bottom-left and bottom-right parts of the image (Fig. 6 and the corresponding Fig. 4B (10)). In the following section, only the slide marked with AB will be analyzed in detail. We take the earliest SAR acquisition date as the reference date, labeled as 20070314 in the first frame of Fig. 6. The numbers in other frames indicate the accumulated days since the first SAR data acquisition. The triangle in the first frame of Fig. 6 is the reference point for SBAS InSAR processing. From the accumulated time-series results, we can see that this slide deformed continuously during each of the monitoring interval.

Accumulated displacements along profile AB in the Boulder Creek landslide are calculated in the line-of-sight direction (Fig. 7). Based on the deformation patterns, this slide can be segmented into three zones along its longitudinal axis: an upper transport zone, a middle accumulation zone, and a lower toe zone (Fig. 7). The maximum motions occur over the middle accumulation zone (Figs. 6 and 7). This

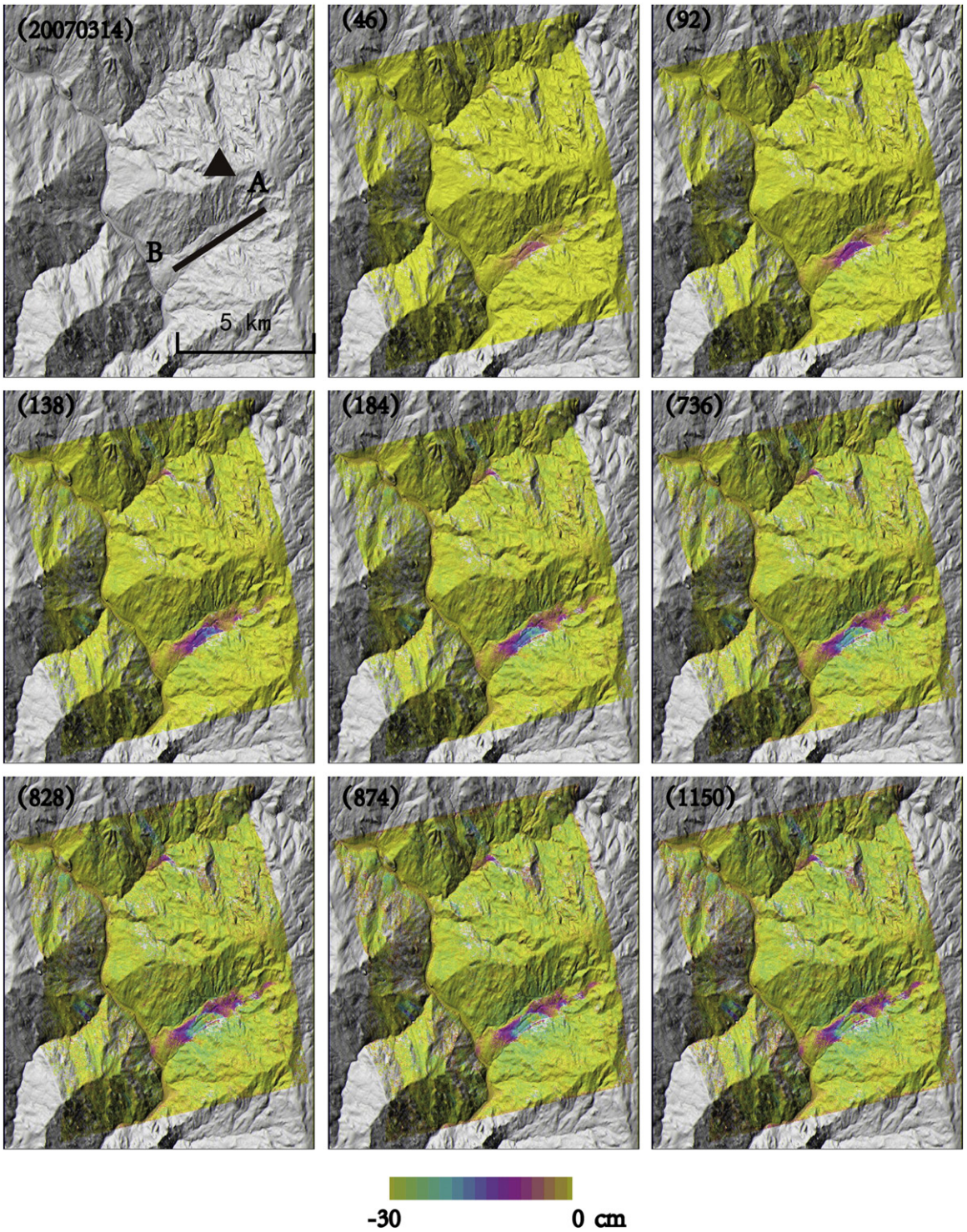

Fig. 6. Maps of time-series deformation at the Boulder Creek slide (labeled as No. 10 in Fig. 4B). The reference SAR acquisition date is 20070314, and the numbers on the subsequent images mark the accumulated days since the reference image. The solid line AB in the first image shows the location of profiles in Figs. 7 and 8. The triangle in the first image indicates the reference point for SBAS InSAR processing.

partition pattern is similar to those previously inferred from aerial photographs in 1944 and 2006 (Stimely, 2009, and references therein). Similar segmentation can also be found at other Eel River slides in California (Mackey et al., 2009).

4.4. Verification of deformation results from adjacent satellite tracks

The azimuth of Boulder Creek slide is about 240° in the downslope direction, and the slope angle is about 14° above the horizontal surface (Stimely, 2009). The azimuth of the ALSO/PALSAR satellite is −9.9°, the incidence angles of track 223 and track 224 at the Boulder Creek slide are 37.2° and 39.8°, respectively. For this slope geometry, a difference of 2.6° in incidence angle between track 223 and track 224 can result in different slope-to-LOS ratios of 2.8 and 2.5, respectively (Eq. 7). Therefore, in order to verify the accuracy of InSAR results, two independent data sets with about the same time interval are shown in Fig. 8. The deformation along the LOS direction and the slope direction are drawn separately for each track.

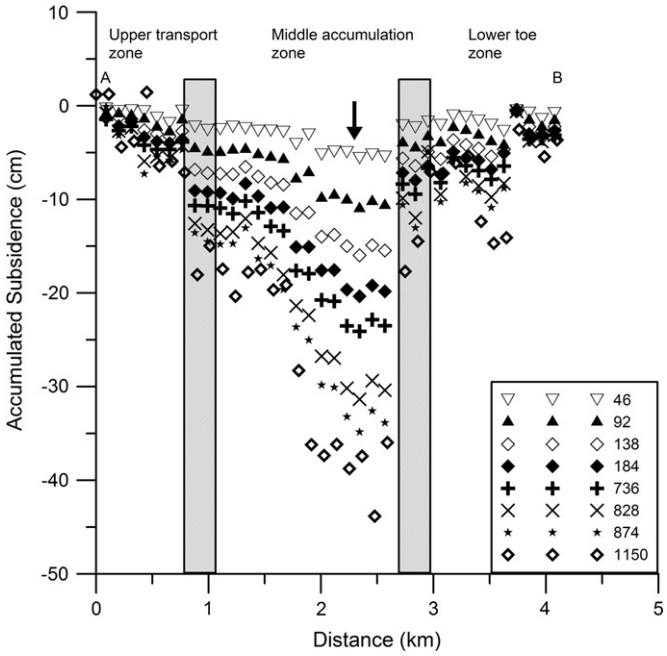

Fig. 7. Cross-section map of the accumulated LOS deformation along the profile AB indicated in Fig. 6.

The LOS deformation from track 223 is similar to that from track 224. However, there exists a systematic difference: the mean LOS deformation from track 224 is generally about 0.54 cm more than the corresponding LOS displacement from track 223 (Fig. 8). However, the difference in downslope displacement between observations from these two tracks only reaches to 0.65 cm. If this difference in down-slope displacement is scaled back to the LOS direction (Eq. 7), the equivalent difference in LOS displacement ranges from 0.23 cm to 0.26 cm, which is half of the original LOS difference (i.e. 0.54 cm). Therefore, most of the difference in LOS displacement can be explained by a difference in SAR look angle between these two adjacent satellite tracks. Meanwhile, the standard deviation of the difference of these two independent measurements is around 0.8 cm, which indicates the accuracy of this InSAR measurement.

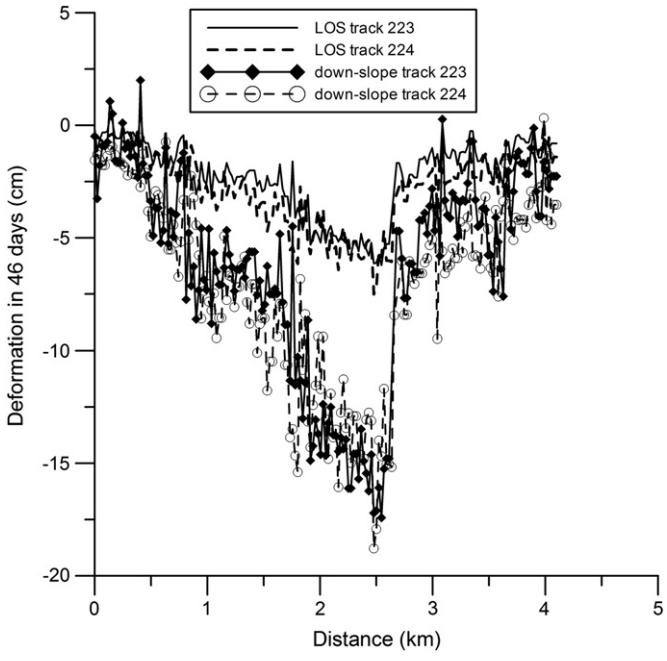

Fig. 8. Landslide deformation patterns across profile A–B based on two 46-day interferograms from track 223 (solid line) and track 224 (dashed line) in the late spring of 2007. The deformation measurements in the down-slope direction (14° above the horizon with an azimuth of 240° from the north) for track 223 and track 224 are plotted with diamonds and circles, respectively.

4.5. Correlation of landslide motion with precipitation

Among the detected landslides of different scales, deformation estimates within 46 days during different time intervals are calculated. The total deformed area approximately amounts to 40 km^2. The LOS deformation in 46 days reached to 6 cm (corresponding to 17 cm in down-slope direction) in spring, and decreased to about 4 cm (corresponding to 11 cm in down-slope direction) in late summer.

Among factors that affect landslide motion such as topography, geology, geotechnical properties, vegetation (including wildfire effects) and anthropogenic development, precipitation is the most dominant factor that controls landslide motion (Fell et al., 2008). We here show the weekly precipitation data collected from Zenia meteorological station (Fig. 1), about 15 km from the Boulder Creek slide (Fig. 9).

In order to analyze the temporal correlation between the landslide movement and the precipitation, the time-series deformation results are normalized into 46 days. The correlation between the down-slope deformed volume change in 46 days and the weekly precipitation at the Boulder Creek slide is shown in Fig. 9. The maximum deformed volume per 46 days occurred at the beginning of 2008, followed by 2009 and 2010. So generally, the more precipitation was, the greater the deformation occurred.

It is interesting to observe that the response of landslide deformation to precipitation is not instantaneous (Fig. 9). Instead, there is a time lag between peak landslide motion and the peak precipitation. At the Boulder Creek slide, the lag is about 1–2 months. Similar findings have been reported for Minor Creek slide in northern California with a lag time of 5–8 days (Iverson, 2000), the Berkeley Hills slide with up to 3 months of lag time (Hilley et al., 2004), and Portuguese Bend landslide in southern California with 2–6 weeks of lag time

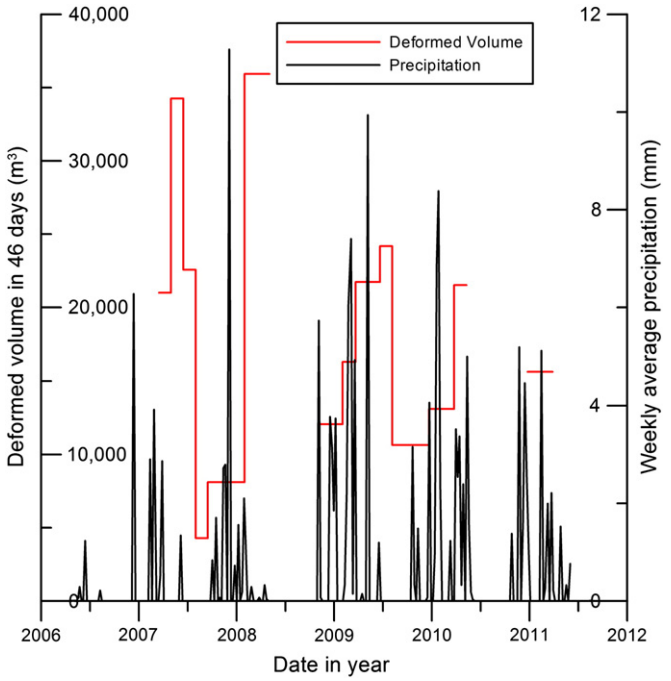

Fig. 9. Correlation between the down-slope deformed volume change in 46 days and the weekly average precipitation data recorded near the Boulder Creek slide.

(Calabro et al., 2010). Due to the low temporal sampling of ALOS/PALSAR data, it is impossible to determine the time lag at a finer temporal resolution. Because of lack of SAR data in early 2007, the exact lag time in 2007 is not obvious either (Fig. 9).

Similar to other landslides in northern California, we attribute the time lag of 1–2 months at Boulder Creek slide to the change of pore pressure since the rainfall. The diffusion of pore pressure generally decreases the normal force and frictional resistance, thereby accelerating the slide movement (Iverson, 2000). Different lag times are mainly related to the slide depth and slope angle. As suggested by previous studies (Nolan & Janda, 1995; Roering et al., 2009), for the deeply sheared melange lithology at a deep-seated landslide such as the Boulder Creek slide, the slope failures move essentially via plug flow along discrete shear zones and are highly controlled by rainfall.

6. Concluding remarks

L-band ALOS/PALSAR data have been successfully used to map active landslides over an area of ~200 km by ~350 km in southern Oregon and northern California, More than 50 active landslides, ranging in size from 0.2 km^2 to more than 10 km^2, comprise a total of 40 km^2. The SBAS InSAR technique has been applied to multi-temporal InSAR images to achieve time-series deformation patterns over each of detected landslides. The results over Boulder Creek slide show three segments along its longitudinal axis in spatial domain. The InSAR accuracy over the Boulder Creek slide can reach to ~1 cm based on InSAR measurements from adjacent tracks. Time-series landslide motions correlate with local precipitation with around 1–2 months lag time between the peak of the precipitation and the maximum deformation rate. Such lags are typical of deep-seated landslides in humid climates and are related to the pore pressure diffusion time since the onset of intense precipitation. Our results will provide an effective method for monitoring and inventorying landslide movement over large areas in the Pacific Northwest, and this approach could facilitate development of early warning systems for slowly moving, deep-seated landslides under abnormal rainfall conditions.

Because L-band InSAR images generally are less sensitive to the surface deformation than C-band and X-band data, landslides with LOS motions of less than ~1 cm in 46–138 days cannot be automatically detected. In addition, it can be difficult to detect slides with motion directions along the satellite flight direction or spatial extents of less than 0.2 km^2. Furthermore, slides with dense vegetation are likely missed due to InSAR coherence loss. Therefore, our results may underestimate the true extents of active landslides over the study region. However, if some knowledge is known, small-scale slides can also be monitored by processing InSAR images at the highest spatial resolution. Obviously, future SAR sensors with higher spatial and temporal resolutions will significantly improve landslide monitoring.

Acknowledgements

The first author would like to thank China Scholarship Council for funding his one-year postdoctoral research at the U.S. Geological Survey (USGS), Cascades Volcano Observatory. ALOS/PALSAR data are copyrighted JAXA/METI and provided by Alaska Satellite Facility through the ALOS Data Consortium. The meteorological data of Zenia station are provided from the website of http://cdec.water.ca.gov/cgi-progs/staMeta?station_id=ZEN. This research is funded by Natural Science Foundation of China (NSFC) (No: 41072266), the Ministry of Land & Resources, China (Nos: 1212011220186 and 121201122014), and USGS Volcano Hazards Program. We thank Hyung-Sup Jung and Chang-Wook Lee for sharing their SBAS codes. Constructive comments from USGS technical reviewer, Tom Pierson, and three anonymous reviewers have improved the manuscript.

References

Berardino, P., Costantini, G., Franceschetti, G., Iodice, L., Pietranera, L., & Rizzo, V. (2003). Use of differential SAR interferometry in monitoring and modeling large slope instability at Matera (Basilicata, Italy). *Engineering Geology*, *68*, 31–51.

Berardino, F., Fornaro, G., Lanari, R., & Sansosti, E. (2002). A new algorithm for surface deformation monitoring based on small baseline differential SAR interferometry. *IEEE Transactions on Geoscience and Remote Sensing*, *40*, 2375–2383.

Bulmer, M. H., Petley, D. N., Murphy, W., & Mantovani, F. (2006). Detecting slope deformation using two-pass differential interferometry: Implications for landslide studies on Earth and other planetary bodies. *Journal of Geophysical Research*, *111*, E06S16, http://dx.doi.org/10.1029/2005JE002593.

Calabro, M. D., Schmidt, D. A., & Roering, J. J. (2010). An examination of seasonal deformation at the Portuguese Bend landslide, southern California, using radar interferometry. *Journal of Geophysical Research*, *115*, F02020, http://dx.doi.org/10.1029/2009JF001314.

Cascini, L., Fornaro, G., & Peduto, D. (2010). Advanced low- and full-resolution DInSAR map generation for slow-moving landslide analysis at different scales. *Engineering Geology*, *112*, 29–42.

Catani, F., Farina, P., Moretti, S., Nico, G., & Strozzi, T. (2005). On the application of SAR interferometry to geomorphological studies: Estimation of landform attributes and mass movements. *Geomorphology*, *66*, 119–131.

Colesanti, C., Ferretti, A., Prati, C., & Rocca, F. (2003). Monitoring landslides and tectonic motions with the Permanent Scatterers Technique. *Engineering Geology*, *68*, 3–14.

Cruden, D. M. (1991). A simple definition of a landslide. *Bulletin of the International Association of Engineering Geology*, *43*, 27–29.

Dai, F. C., Lee, C. F., & Ngai, Y. Y. (2002). Landslide risk assessment and management: An overview. *Engineering Geology*, *64*, 65–87.

Ding, X., Montgomery, S. B., Tsakiri, M., Swindells, C. F., & Jewell, R. J. (1998). Integrated monitoring systems for open pit wall deformation. *Australian Centre for Geomechanics, ACG: 1005-98, Meriwa Report No.186, Perth, Australia* (pp. 3–114)., http://dx.doi.org/10.1007/s00254-008-1654-9.

Farina, P., Colombo, D., Fumagalli, A., Marks, F., & Moretti, S. (2006). Permanent scatterers for landslide investigations: Outcomes from the ERS-SLAM project. *Engineering Geology*, *88*, 200–217.

Farr, T. G., et al. (2007). The shuttle radar topography mission. *Reviews of Geophysics*, *45*, RG2004, http://dx.doi.org/10.1029/2005RG000183.

Fell, R., Corominas, J., Bonnard, C., Cascini, L., Leroi, E., & William, Z. S. (2008). Guidelines for landslide susceptibility, hazard and risk zoning for land-use planning. *Engineering Geology*, *102*, 99–111.

Ferretti, A., Monti, G. A., Prati, C., Rocca, F., & Massonnet, D. (2007). InSAR principles: Guidelines for SAR interferometry processing and interpretation(TM-19, February 2007). ESTEC, Postbus 299, 2200 AG Noordwijk, the Netherlands: ESA Publications.

Ferretti, A., Prati, C., & Rocca, F. (2001). Permanent scatterers in SAR interferometry. *IEEE Transactions on Geoscience Remote Sensing*, *39*, 8–20.

Fu, X., Guo, H., Tian, Q., & Guo, X. (2010). Landslide monitoring by corner reflectors differential interferometry SAR. *International Journal of Remote Sensing*, *31*, 6387–6400.

Gesch, D. (1994). Topographic data requirement for EOS global change research. *U.S. Geol. Surv. Open-File Rpt* (pp. 94–626)..

Hanssen, R. (2001). Radar interferometry: Data interpretation and error analysis. Netherlands: Kluwer Academic Publishers.

Hilley, G. E., Burgmann, R., Ferretti, A., Novali, F., & Rocca, F. (2004). Dynamics of slow-moving landslides from permanent scatterer analysis. *Science*, *304*, 1952–1955.

Iverson, R. M. (2000). Landslide triggering by rain infiltration. *Water Resources Research*, *36*, 1897–1910.

Iverson, R. M., & Major, J. J. (1987). Rainfall, groundwater flow, and seasonal movement at Minor creek landslide, northwestern California: Physical interpretation of empirical relations. *Geological Society of America Bulletin*, *99*, 579–594.

Lanari, R., Mora, O., Mununta, M., Mallorqui, J., Berardino, P., & Sansosti, E. (2004). A small baseline approach for investigating deformation on full resolution differential SAR interferograms. *IEEE Transactions on Geoscience and Remote Sensing*, *42*, 1377–1386.

Lee, C. W., Lu, Z., Jung, H. S., Won, J. S., & Dzurisin, D. (2010). Surface deformation of Augustine Volcano (Alaska), 1992–2005, from multiple-interferogram processing using a refined SBAS InSAR approach, chapter 18 of Power, J.A.. In M. L. Coombs, & J. T. Freymueller (Eds.), *The 2006 eruption of Augustine Volcano, Alaska: U.S. Geological Survey Professional Paper 1769* (pp. 453–465). , http://pubs.usgs.gov/pp/1769/chapters/p1769_chapter18.pdf

Leva, D., Nico, G., Tarchi, D., Fortuny, G. J., & Sieber, A. J. (2003). Temporal analysis of a landslide by means of a ground-based SAR interferometer. *IEEE Transactions on Geoscience and Remote Sensing*, *41*, 745–752.

Lu, Z., Dzurisin, D., Jung, H. S., Zhang, J. X., & Zhang, Y. H. (2010). Radar image and data fusion for natural hazards characterization. *International Journal of Image and Data Fusion*, *1*, 217–242.

Mackey, B., Roering, J. J., & McKean, J. A. (2009). Long-term kinematics and sediment flux of an active earthflow, Eel River, California. *Geology*, *37*, 803–806.

Massonnet, D., & Feigl, K. L. (1998). Radar interferometry and its application to changes in the Earth's surface. *Review of Geophysical*, *36*, 441–500.

Mora, O., Mallorqui, J. J., & Broquetas, A. (2003). Linear and nonlinear terrain deformation maps from a reduced set of interferometric SAR images. *IEEE Transactions on Geoscience and Remote Sensing*, *41*, 2243–2253.

Nolan, K. M., & Janda, R. J. (1995). Movement and sediment yield of two earthflows, northwestern California. In K. M. Nolan (Ed.), *Geomorphic Processes and Aquatic Habitat in the Redwood creek Basin, Northwestern California* (pp. 1454-F). : U. S. Geol. Surv. Prof F1-F12.

Parise, M. (2001). Landslide mapping techniques and their use in the assessment of the landslide hazard. *Physics and Chemistry of the Earth Part C: Solar, Terrestrial & Planetary Science*, *26*, 697–703.

Pierson, T., & Lu, Z. (2009). InSAR detection of renewed movement of a large ancient landslide in the Columbia River Gorge, Washington. (abst.). *From volcanoes to vineyards: Living with dynamic landscapes: Abstracts with programs, v.41, no. 7, Geological Society of America 2009 Annual Meeting* (pp. 497).

Roering, J. J., Stimely, L. L., Mackey, B. H., & Schmidt, D. A. (2009). Using DInSAR, airborne LiDAR, and archival air photos to quantify landsliding and sediment transport. *Geophysical Research Letters*, *36*, L19402, http://dx.doi.org/10.1029/2009GL040374.

Rosen, P., Hensley, S., Zebker, H., Webb, F. H., & Fielding, E. J. (1996). Surface deformation and coherence measurements of Kilauea volcano, Hawaii, from SIR-C radar interferometry. *Journal of Geophysical Research*, *101*, 23109–23125.

Samsonov, S., van der Kooij, Marco, & Tiampo, K. (2011). A simultaneous inversion for deformation rates and topographic errors of DInSAR data utilizing linear least square inversion technique. *Computers and Geosciences*, http://dx.doi.org/10.1016/j.cageo.2011.01.007.

Sandwell, D., Myer, D., Mellors, R., Masanobu, S., Benjamin, B., & James, F. (2008). Accuracy and resolution of ALOS interferometry: Vector deformation maps of the Father's Day Intrusion at Kilauea. *IEEE Transactions on Geoscience and Remote Sensing*, *46*, 3524–3534.

Sansosti, E., Casu, F., Manzo, M., & Lanari, R. (2010). Space borne radar interferometry techniques for the generation of deformation time series: An advanced tool for Earth's surface displacement analysis. *Geophysical Research Letter*, *37*, L20305, http://dx.doi.org/10.1029/2010GL044379.

Schmidt, D., & Burgmann, R. (2003). Time-dependent land uplift and subsidence in the Santa Clara Valley, California, from a large interferometric synthetic aperture radar data set. *Journal of Geophysical Research*, *108*(B9), 2416, http://dx.doi.org/10.1029/2002JB002267.

Stimely, L. L. (2009). Characterizing Landslide Movement at the Boulder creek Earthflow, Northern California, Using L-band InSAR, Master thesis in the Department of Geological Sciences and the Graduate School of the University of Oregon, Eugene.

Strozzi, T., Farina, P., Corsini, A., Ambrosi, C., Thüring, M., Zilger, J., et al. (2005). Survey and monitoring of landslide displacements by means of L-band satellite SAR interferometry. *Landslides*, *2*, 193–201.

Thompson, P. W., & Cierlitza, S. (1993). Identification of a slope failure over a year before final collapse using multiple monitoring methods. In T. Szwedzicki (Ed.), *Geotechnical instrumentation and monitoring in open pit and underground mining* (pp. 491–511). Netherlands: A.A. Balkema, Rotterdam.

Vladimir, G., & Jan, V. (2011). Monitoring of post-failure landslide deformation by the PS-InSAR technique at Lubietova in Central Slovakia. *Environmental Earth Science*, http://dx.doi.org/10.1007/s12665-011-0951-x.

Xia, Y., Kaufmann, H., & Guo, X. F. (2004). Landslide monitoring in the Three Gorges area using D-INSAR and corner reflectors. *Photogrammetric Engineering and Remote Sensing*, *70*, 1167–1172.

Yun, S. H., Zebker, H., Segall, P., Hooper, A., & Poland, M. (2007). Interferogram formation in the presence of complex and large deformation. *Geophysical Research Letter*, *34*, L12305, http://dx.doi.org/10.1029/2007GL029745.

Zebker, A. H., & Chen, K. (2005). Accurate estimation of correlation in InSAR observations. *IEEE Transactions on Geoscience and Remote Sensing letters*, *2*, 124–127.

Zebker, A. H., & Villasenor, J. (1992). Decorrelation in interferometric radar echoes. *IEEE Transactions on Geoscience and Remote Sensing*, *30*, 950–959.